Hindawi
Geofluids
Volume 2022, Article ID 7746386, 12 pages
https://doi.org/10.1155/2022/7746386

Research Article

Methane Flux Effect on Hydrate Formation and Its Acoustic Responses in Natural Sands

Qingtao Bu[1,2] **Tongju Xing**[3,4] **Gaowei Hu**[1,2] **Changling Liu**[1,2] **Chengfeng Li**[1,2] **Jinhuan Zhao**[1,2] **Zihao Wang**[1] **Wengao Zhao**[1] **and Jiale Kang**[1]

[1]*Key Laboratory of Gas Hydrate, Ministry of Natural Resources, Qingdao Institute of Marine Geology, Qingdao 266237, China*
[2]*Laboratory for Marine Mineral Resources, Qingdao National Laboratory for Marine Science and Technology, Qingdao 266237, China*
[3]*Qingdao Geo-Engineering Surveying Institute (Qingdao Geological Exploration and Development Bureau), Qingdao 266100, China*
[4]*Key Laboratory of Geological Safety of Coastal Urban Underground Space, Ministry of Natural Resources, Qingdao 266100, China*

Correspondence should be addressed to Qingtao Bu; bqt881110@163.com and Gaowei Hu; hgw-623@163.com

Received 7 October 2021; Accepted 4 May 2022; Published 30 May 2022

Academic Editor: Mohammed Fattah

The acoustic properties of hydrate deposits are important parameters for hydrate geophysical exploration, and the gas leakage model plays a very important role in hydrate accumulation systems. In order to reflect the gas supply environment during hydrate formation, a high-pressure device with a simulated leakage system was designed to achieve different methane flux supplies. The effects of different methane fluxes on the hydrate formation rate and the maximum hydrate saturation were obtained. The results in this study indicate that similar hydrate formation rates occur in systems with different methane fluxes. However, when the methane flux is large, it takes longer to reach the maximum hydrate saturation, and the larger the methane flux, the larger the hydrate saturation formed. In each methane flux system, the elastic velocity increased slowly with increasing hydrate saturation at the beginning of hydrate formation, but velocity increased quickly when the hydrate saturation reached 50–60%. In order to take into account the effect of the gas, the calculated values of the elastic velocity model were compared with the experimental data, which indicated that the BGTL theory and the EMT model are more adaptable and can be used to deduce hydrate morphology. In the large methane flux system, the hydrate mainly forms at grain contacts when the hydrate saturation is 10–60%. As the hydrate saturation reaches 60–70%, hydrate forms first in the pore fluid, and then the hydrates contact sediment particles.

1. Introduction

Natural gas hydrates are considered to be very promising potential clean energy sources in the future [1, 2]. Geophysical exploration methods remain the primary means of exploring for marine gas hydrates [3]. Hydrate-bearing sediments exhibit higher acoustic velocities compared to background sediments [4, 5], and the presence of hydrates will affect the physical properties of the reservoir [6–9]. When the temperature and pressure conditions exceed the phase equilibrium conditions, hydrates are difficult to preserve. Therefore, it is not very clear how wave velocities vary with the saturation of hydrate. Simulation experiment in the laboratory is an effective way to obtain data to understand the link between the velocity and saturation.

In recent years, a variety of detection methods have found that methane flux is an important controlling factor for hydrate formation. The methane leakage system plays an important role in the formation of hydrate. Mahabadi et al. [10] simulated the migration and capture of bubbles using pore network models extracted from 3D images of in situ sediments. The results show that the distribution of bubble size becomes wider with bubble transport as the bubbles are coalescing. Methane release from temperature-induced hydrate decomposition in the West Svalbard continental margin was studied by Thatcher et al. [11]. Wang et al. [12] used magnetic resonance imaging (MRI) to observe the formation and decomposition of hydrates in dynamic conditions. It was found that the optimal gas migration rate

resulted in the maximum hydrate saturation in porous media and the gas upward migration system ratio. The downward gas transport system can change the spatial structure of porous media more. The scale of methane flux is one of the most important factors influencing the hydrate formation process. Different seepage fluxes will influence the rate of hydrate formation, the amount of hydrocarbon accumulation, and the occurrence of hydrate deposits. It is helpful to further understand the formation characteristics of leakage hydrates by simulating the formation of hydrate in different methane fluxes.

Currently, most experimental studies on the acoustic characteristics of hydrate reservoirs have been conducted in static experimental systems. Priest et al. [13, 14] focused on how hydrate affects wave velocity under different gas-to-water ratios. Winters et al. [15] investigated how hydrate affects wave velocity in different sediments. Hu [16–19] investigated the formation and decomposition of hydrate in consolidated and unconsolidated sediments, and Hu et al. [4] and Bu et al. [5] also studied hydrate dissociation characteristics in sediments from the South China Sea. Andhumoudine et al. [20] also studied the elastic properties of coal based on digital core technology and finite element method. It is not easy to conduct experiments on formation of hydrate in a dynamic gas leakage system. Few experimental studies of gas leakage systems have been performed, and hydrate generation experiments are difficult for different methane flux modes. Most prior experiments were conducted using a single methane flux, and only a small number of experiments studied the acoustic properties. Gao et al. [21] studied the kinetic process of methane hydrate formation under confining pressures, they developed a novel triaxial horizon fixed bed reactor, and obtained the influence of several key factors (i.e., water-gas ratio, pressure, temperature and the presence of NaCl) on the kinetic behavior of methane hydrate formation. The evolution of gas and water profiles and triaxial pressure in the process of hydrate dissociation have also been studied [22]. They also conducted a multi-stage depressurization to adjust the fluid production behavior of hydrate sediments and obtained good results [23]. An experimental setup was developed to simulate a real depositional system [24], with a water inflow at the top and a gas inflow at the bottom, and the experimental setup is capable of acoustic velocity detection. Kwon and Cho [25] did CO_2 hydrate generation experiments by fluid injection and obtained acoustic parameters during the experiments. Liu et al. [26] conducted hydrate generation experiments and tested acoustic velocities in a CH_4-CO_2 replacement reaction apparatus, which was a gas dynamic transport system. Guan et al. [27] simulated the formation process of gas hydrate in a gas leakage system, and tested the relevant physical parameters. A special high-pressure device was designed by Bu et al. [28] to study the effect of gas on hydrate saturation and velocities during vertical gas migration conditions. However, they did not quantify the methane flux during the experiment process. Most of the above studies were carried out in closed reaction vessels, therefore it is not possible to characterize the migration of gas in the sediment during hydrate formation.

In order to reflect the formation of hydrate under gas leakage conditions, a simulator was designed to realize hydrate formation in sediments under various methane flux conditions, using an additional gas flow control system to control the methane supply. The waveform data and water content were obtained by combining ultrasonic techniques with time domain reflection (TDR). The data were then used to study the variations in hydrate saturation and the correlation between velocity and saturation as a function of methane flux.

2. Experiment

2.1. Experimental Facilities and Materials. The hydrate simulation experimental setup consists of five parts: high-pressure reactor and gas distribution section, pressure control section, refrigeration section, gas flow rate control section, and test section (Figure 1). For a detailed description of the specifics of the experimental setup refer to reference [29]. Figure S5 in the Supplementary Materials exhibits the inner of the apparatus, especially for the microporous sintered plate.

In a previous study, several methods were used to simulate the formation of hydrate in a gas migration system [23]. Based on this gas migration system, a BROOKS mass flow controller was applied to the gas path to achieve gas flow control in the reaction system. Experiments were then carried out under different methane flux supply modes, and the influence of different methane fluxes on the hydrate saturation and its acoustic response characteristics were studied by a series of experiments.

As the BROOKS mass flow controller needs a constant gas pressure for the measurement, a TESCOM manual pressure-reduction valve and a manual back-pressure valve were used in the flow measurement set-up before and after the installation, and the gas pressure was maintained at 29 MPa (which is the maximum pressure of the mass flow controller). Under this condition, the flow measurement and control meter can achieve the expected measurement and control accuracy. In order to automatically switch the mass flow controller between different flows, a pneumatic ball valve was installed on the gas piping between the controller outlet and the back-pressure valve inlet. The control system automatically selects the appropriate flow meter, and opens or cuts off the gas line, depending on the flow rate. The ball valve was placed in the controller outlet in order to protect the controller from the impact of pressure and the impact of the direction pressure. After the gas moves across the pressure-reducing valve, the mass flow controller, the gas-control ball valve, and the back-pressure valve, the gas pressure is maintained at the preset pressure (less than 20 MPa) and introduced into the experimental system by a TESCOM pneumatic control valve.

For the experiment, the sand particle size is 0.15–0.30 mm [30], the solution used for the experiments was a 0.03% concentration of sodium dodecyl sulfate solution. The gas used in the experiments was pure CH_4 gas, the concentration of CH_4 gas was 99.9%.

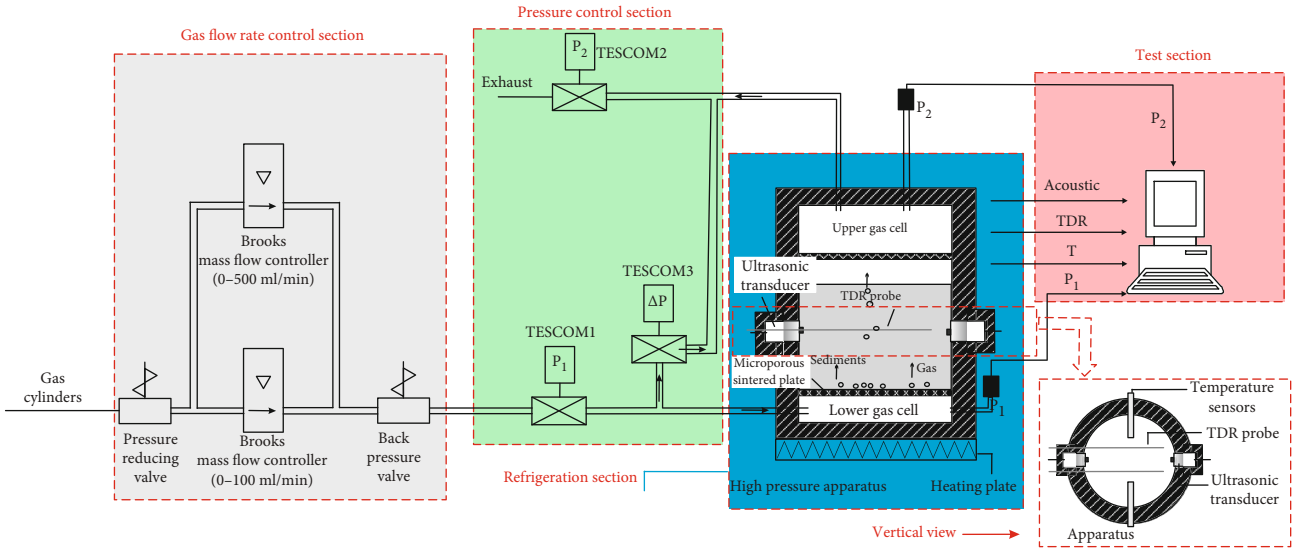

FIGURE 1: An experimental device for gas hydrate formation and acoustic velocity detection with different methane flux (Modified from [29]).

2.2. Experimental Method and Procedure. In this experiment, we still use ultrasonic detection and TDR detection to obtain acoustic wave travel time and water content [5, 18]. The detailed measuring method of the acoustic data and hydrate saturation are described in Text S1 and S2 in the Supplementary Materials.

The P-wave velocity and S-wave velocity are determined by equations (1) and (2):

$$V_p = \frac{L}{t_p - t_{0p}} \tag{1}$$

$$V_s = \frac{L}{t_s - t_{0s}} \tag{2}$$

Here, L represents the detection length between the sensors, t_{0p} and t_{0s} represent the Intrinsic propagation time of the sensors, and t_p and t_s represent the times of the P- and S- waves. Figure S1–S3 and Table S1–S2 in the Supplementary Materials exhibit the Calibration of the ultrasonic transducers.

For hydrate deposits, the main application is the model of Wright et al. [31]:

$$\theta_v = -11.9677 + 4.506072566K - 0.14615K^2 + 0.0021399K^3 \tag{3}$$

Here, θ_v represents the water content, and K represents the dielectric constant, Figure S4 and Table S3 in the Supplementary Materials exhibit the calibration of the TDR probes. And we can calculate the hydrate saturation according to the water content (θ_v) and porosity (φ) of the samples:

$$S_h = (\varphi - \theta)/\varphi \times 100\% \tag{4}$$

In this study, we use X-rays to transmit through the test sample. The X-ray CT images were obtained using the different absorption of the rays by the substances. The different densities and thicknesses of the components, allowed us to obtain information on the distribution of each component in the CT images [5].

The experiment steps for gas hydrate formation with different methane fluxes were:

(1) Firstly, the different sensors are positioned in the reactor in the right place

(2) Methane gas was introduced into the reactor and pressurized to 6 MPa. Set a pressure difference of 0.3-0.5 MPa in the reactor

(3) Depending on the requirements of different experimental cases, the mass flow controller was set in the range of 0-500 ml/min to achieve the required control of methane flow

(4) After the reactor was installed, turn on the temperature control system and control the temperature of the whole experimental system to 2°C

(5) When the pressure in the reactor remained constant for a long time, it was considered that the hydrate was no longer generated, and the cooling system was shut down, and then increasing the temperature so that the hydrate began to dissociate

The CT scanning experiment procedure during hydrate formation stage with methane flux was as follows.

(1) The sand and 3.5 wt.% NaCl solution are loaded into the reaction chamber for CT scanning, the sample chamber is connected to the gas migration system, the gas enters from the lower part of the sample chamber and flows out from the upper part

Table 1: Effect of methane flux on hydrate formation.

Run no.	Gas flux mode/(ml/min)	T/°C	Upper gas cell pressure/MPa	Lower gas cell pressure/MPa	Maximum hydrate saturation/%	V_s (m/s)	V_p (m/s)
1	30	2.25	3.46	3.51	71.4	1291	2670
2	30	3.06	3.77	3.78	71.4	1287	2674
3	30	2.09	3.22	3.26	71.4	1285	2668
4	60	4.07	4.52	4.54	74.2	1328	2722
5	60	3.90	4.82	4.84	74.2	1327	2721
6	60	3.58	5.53	5.54	74.2	1332	2735
7	200	1.61	5.70	6.57	82.7	1531	3150
8	200	1.95	5.18	6.11	82.7	1535	3167
9	200	1.55	6.09	6.38	82.7	1533	3153
10	400	2.52	6.11	6.12	90.9	1638	3298
11	400	3.02	6.15	6.31	90.9	1618	3287
12	400	2.72	6.05	6.11	90.9	1635	3293

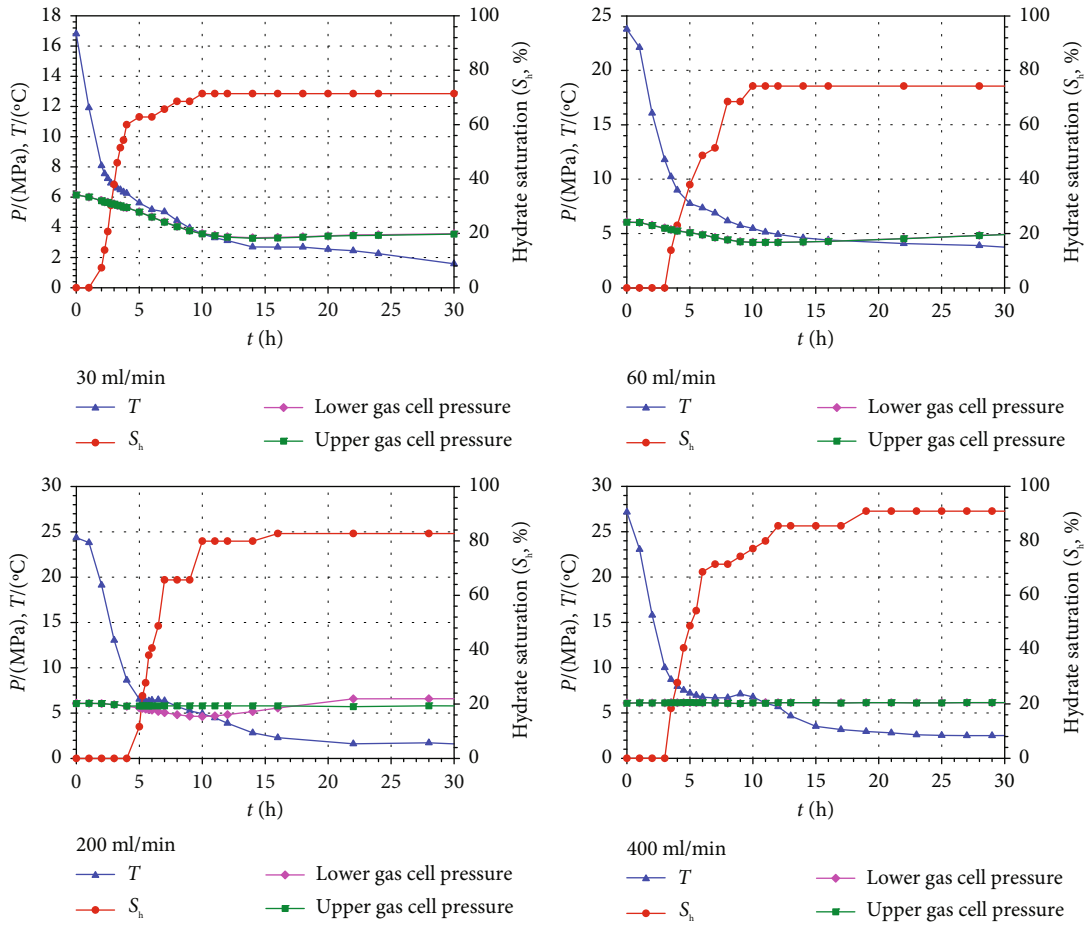

Figure 2: Variation in temperature, pressure and hydrate saturation (S_h) during gas hydrate formation in different methane fluxes (Data for Figure 2 are in Table S4 in the Supplementary Materials). (Methane flow rate: 30 ml/min、60 ml/min、200 ml/min、400 ml/min).

(2) Inject methane gas into the reactor, control the upper and lower gas pressure difference at 0.3 MPa, realize the gas migration from the bottom to the upper part, and control the pressure of the reactor at 6.5 MPa

(3) Turn on the cooling system and begin to form hydrates. In the different stages of hydrate formation process, when X-CT scanning is required, the gas inlet and outlet of the reaction chamber are closed,

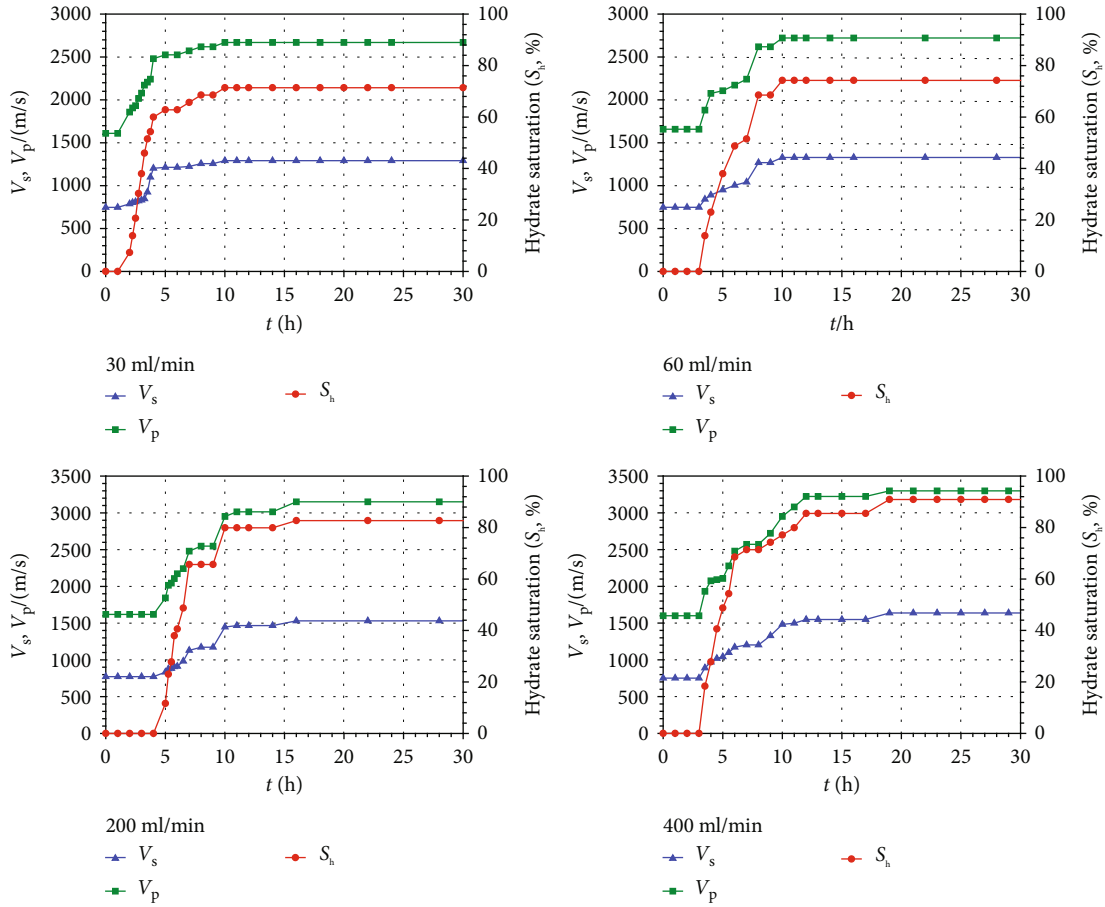

FIGURE 3: Variation in hydrate saturation and wave velocity during hydrate formation (30 ml/min、60 ml/min、200 ml/min、400 ml/min), (Data for Figure 3 are in Table S5 in the Supplementary Materials).

and the reaction kettle is transferred to the CT laboratory instrument for scanning

(4) The variation of distribution and pore morphology of each component with methane flux was observed. For more information about the steps of CT analysis, please refer to reference [32, 33].

In this study, acoustic experiments on hydrate-bearing sediments under different methane flux conditions and X-CT scanning cannot be performed simultaneously, so when performing X-CT scanning observations, we only performed scanning observations under different pressure conditions to help analysis.

3. Results

3.1. Hydrate Formation Process. Due to the limitations of laboratory simulation scales, it is not possible to simulate a large range of methane fluxes as in the field. Methane flow rates of 30 ml/min, 60 ml/min, 200 ml/min, and 400 ml/min were carried out in a multi-cycle simulation experiment under different methane flux supply modes. 12 experiment runs were conducted (Table 1) and one run of experimental data from each flux mode was selected for analysis. The observed variations in pressure, temperature, and hydrate saturation during the experiment process are shown in Figure 2.

As the experiment was conducting, the pressure of the apparatus was decreased before the maximum saturation of the hydrate was reached in the 30 ml/min and 60 ml/min modes. This indicates that for the 30 ml/min and 60 ml/min methane supply modes, the methane consumption rate was higher than the methane supply rate. With the onset of hydrate formation, methane consumption was gradually reduced. When the maximum hydrate saturation was reached and the saturation no longer increased, the internal pressure in the chamber gradually increased. When the methane supply was controlled at 200 ml/min, there were only small fluctuations in the lower gas chamber of the reactor, indicating that the 200 ml/min supply rate was comparable to the methane consumption rate during hydrate formation. When the methane supply was controlled at 400 ml/min, the pressure did not change substantially, indicating that the gas supply rate equaled the methane consumption during hydrate formation and maintained the pressure. From Figure 2, an abnormal temperature point can be observed during the formation of hydrate. Although hydrate formation generally occurs as temperature decreases, when the hydrate first formed in the experiment,

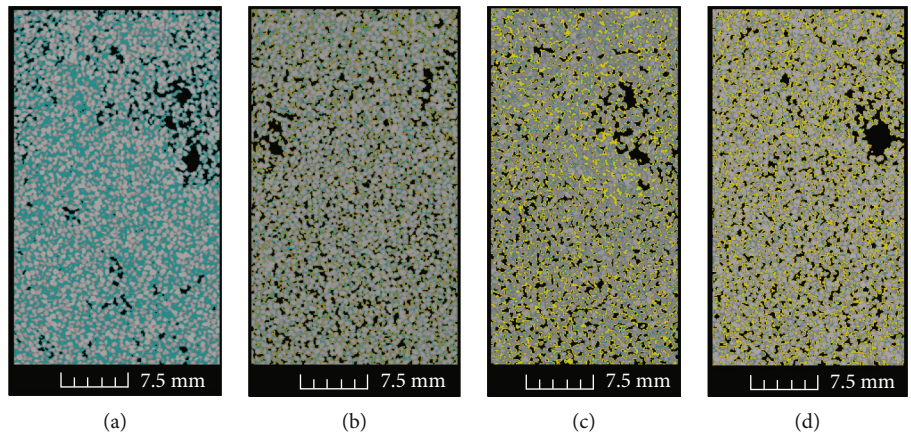

Figure 4: Micro-distribution of gas hydrate during hydrate formation process under methane flux conditions. (a) Hydrate saturation =0%, (b) Hydrate saturation =22.13%, (c) Hydrate saturation =47.33%, (d) Hydrate saturation =59.87%. The yellow is methane hydrate. The blue is NaCl solution. The light gray is sands. The black is methane gas.

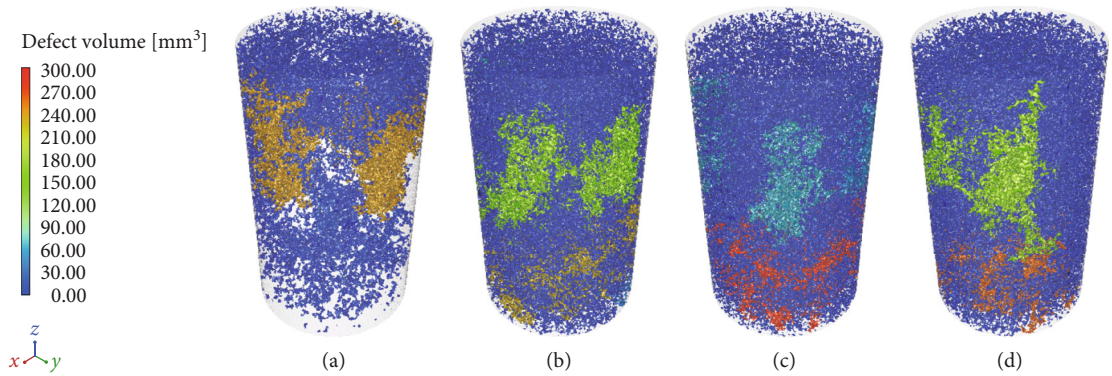

Figure 5: Extracted gas distribution during hydrate formation process under methane flux conditions. (a) Gas ratio =5.35%, (b) Gas ratio =11.65%, (c) Gas ratio =11.99%, (d) Gas ratio =11.35%. Different colors represent the size of the gas volume.

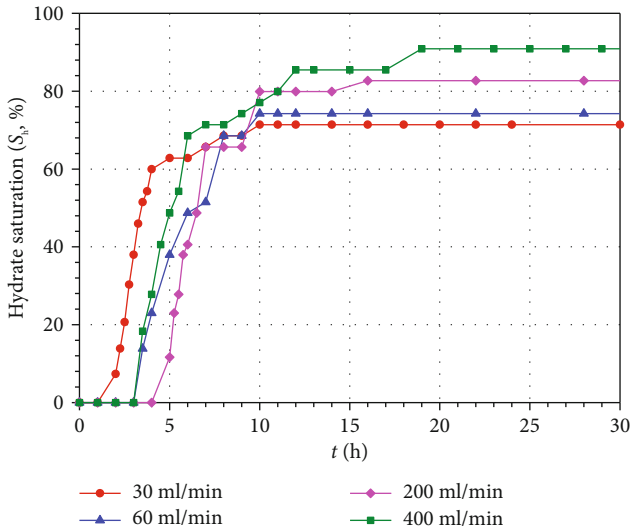

Figure 6: Effect of methane flux on hydrate formation (Data for Figure 6 are in Table S6 in the Supplementary Materials).

the temperature was unusually elevated due to the exothermic process. Such temperature anomalies are present in the four different methane flux modes, but vary little between the 30 ml/min and 60 ml/min flow rate modes with slight fluctuations. Very obvious temperature anomalies can be seen from the 200 ml/min and 400 ml/min flow rate modes. This may be because more hydrate forms in the larger methane flux mode than in the smaller methane flux mode, resulting in a large temperature fluctuation during the temperature drop.

Table 2: Effect of methane flux on hydrate formation rate and hydrate saturation.

Gas flux	Time	Maximum hydrate saturation
30 ml/min	10 h	71.4%
60 ml/min	10 h	74.2%
200 ml/min	16 h	82.7%
400 ml/min	19 h	90.9%

3.2. Variation of Wave Velocity under Different Methane Flux Conditions. For the different methane flux modes, 12 experiment runs were conducted. The results show that each experiment has good repeatability, indicating that the equipment is stable and reliable. Here, we illustrate the results with an example. When gas hydrate formed in the system,

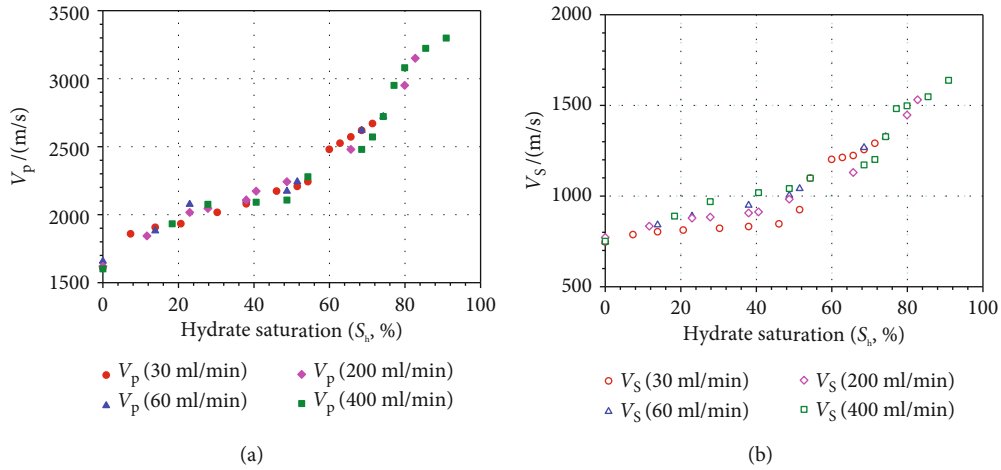

Figure 7: Variation in wave velocities with hydrate saturation in different methane flux. (a) Variation of P-wave velocity. (b) Variation of S-wave velocity (Data for Figure 7 are in Table S7 in the Supplementary Materials).

the detected wave velocities increased as hydrate saturation increasing, and the trend is basically the same (Figure 3). In the non-hydrate sediments, the P-wave velocities were 1601–1657 m/s and the S-wave velocities were 746–771 m/s. Due to the different amounts of hydrate formation at different methane fluxes, larger saturation of the hydrate results in larger wave velocities. Under the condition of 30 ml/min methane supply, the hydrate saturation reached 71% and the P-wave velocity reached 2669 m/s and the S-wave velocity was 1291 m/s. When the methane flux was 400 ml/min, the hydrate saturation reached 90.9%, the P-wave velocity was 3298 m/s and the S-wave velocity reached 1638 m/s.

3.3. The Morphology of Hydrate and Gas during Hydrate Formation Process under Methane Flux Conditions. The diameter of the experimental sample is 25 mm and the height is 50 mm. This study mainly considers the influence of gas flux, so we intercept almost the entire sample size for analysis. The hydrate saturation data is obtained by analyzing the reconstructed three-dimensional image through X-CT technology, and calculating the proportion of hydrate in the selected area [5]. The micro-distribution of the samples was observed at different moments during the formation of hydrate (Figure 4), the hydrate saturation is 0%, 22.13%, 47.33%, and 59.87%, respectively. Under the condition of gas flux, it can be clearly observed from Figure 4 that the spatial distribution of gas in the sediment varies during the different formation stages of hydrate, and the methane gas is not constant in one position. In order to better observe the gas distribution in different stages of hydrate formation, we extracted the gas in different stages separately and obtained the statistical gas volume size. Before the formation of hydrate, the proportion of gas was 5.35% (Figure 5(a)), and gas clusters were distributed on the upper part of the sediment. With the formation of hydrate, the proportion of gas in the entire system gradually stabilized, and it can be clearly observed that the volume of a single gas is getting larger, and a channel of methane gas is formed from bottom to top in the sediment (Figure 5).

4. Discussion

4.1. Effect of Methane Flux on Hydrate Formation Rate and Hydrate Saturation. The effects of different methane fluxes on hydrate formation rates and maximum hydrate saturation were obtained from the experiments (Figure 6, Table 2). Under different methane flux conditions, where the saturation of the hydrate changes with time, the slope of each curve is similar, which indicates that the hydrate formation rates are similar under different conditions. At low methane flow rates (30 ml/min and 60 ml/min gas flow rate), the maximum saturation was reached at 10 h, and at 16 h at a flow rate of 200 ml/min, while at 400 ml/min gas flow rate, 19 h was needed to reach the maximum hydrate saturation. It is shown that the smaller the methane flux was, the less time was required to generate the maximum hydrate saturation under the experimental conditions, and the larger the methane flux was, the longer the time required to reach the maximum hydrate saturation. The hydrate saturation reached 71.4% at a gas flow rate of 30 ml/min. When the inlet flow rate was increased to 400 ml/min, the hydrate saturation was 90.9%. Thus, the larger the methane flux, the easier it is to form high-saturation hydrate.

4.2. Hydrate Saturation Changes with Wave Velocities and Velocity Model Verification. Using the obtained experimental data, correlation of hydrate saturation and acoustic velocity at different methane flow rates was established (Figure 7). It is showed that the wave velocities increase gradually as hydrate saturation increasing. The different methane flux patterns show a more consistent trend. When the hydrate began to form, the wave velocity exhibits a relatively rapid growth. In the hydrate formation stage, the wave velocities show a relatively gentle growth trend. At a hydrate saturation of 50–60%, the rate of increase in the wave velocities is significantly larger.

Comparing the calculated values of the velocity model with the experimental values in the BGTL theory (Figure 8), the parameters used in the model are shown in

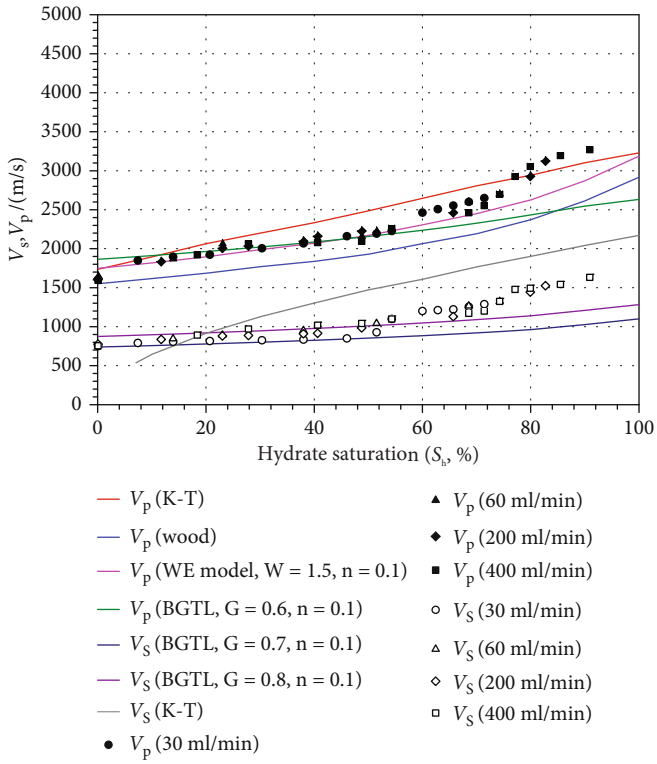

Figure 8: Variation of measured and model-calculated V_p and V_s with hydrate saturation (Data for Figure 8 are in Table S8 in the Supplementary Materials).

Table 3: Mineral composition and physical parameters of the experimental sediments [34–36].

Mineral	Content(%)	ρ(g/cm^3)	K(Gpa)	G(Gpa)
Magnetite	1.94	5.21	161	91.4
Amphibole	1.10	3.12	87	43
Epidote	0.55	3.4	106.2	61.2
Quartz	38.95	2.65	36.6	45
Feldspar	57.46	2.62	76	26
Water		1.032	2.5	0
Pure hydrate		0.9	5.6	2.4
Gas		0.235	0.1	0

Table 3. When G =0.6 and n =0.1, and the hydrate saturation is 0–50%, the predicted P-wave velocity is similar to the measured value. When G =0.7, n =0.1 and G =0.8, and n =0.1, the S-wave velocity predicted by BGTL is close to the experimental value when the hydrate saturation is 0–50%. In the weight equation, when W =1.5 and n =0.1, the predicted P-wave velocity tends to be similar to the experimental value, but there is a certain difference between the calculated value and the actual value. The results of the Wood equation and the K-T equation are different from those of the experimental value, and are not suitable for estimating the velocity in this system.

In addition to the above models, there is a more important equivalent theoretical model for the study of the velocity model of hydrate reservoirs. The effective medium theory

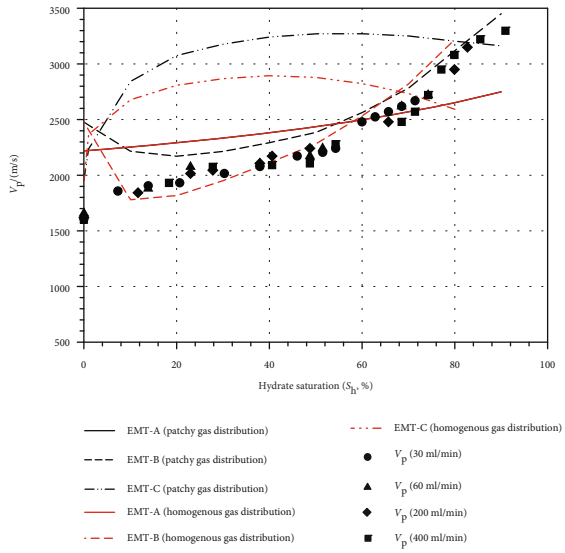

Figure 9: Variation of measured V_p and the calculated V_p from the EMT model with hydrate saturation (Data for Figure 9 are in Table S9 in the Supplementary Materials).

(EMT) [34, 35] is suitable in this study. In previous research, we considered the influence of gas on the wave velocity of hydrate sediments and verified the relevant models [29].

The microscopic distribution pattern of hydrate will affect the flow characteristics and acoustic properties of the reservoir [5, 37]. For example, to explain the effects of creep microstructure and axial strain on the permeability of

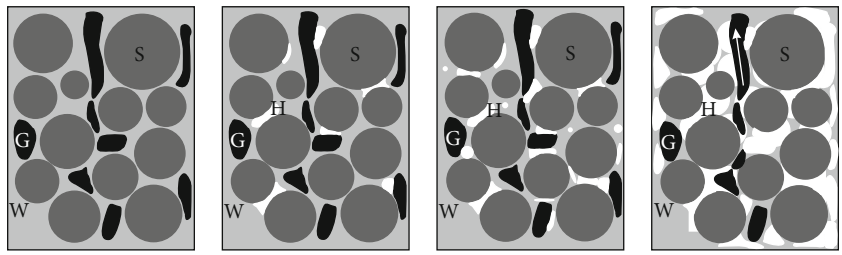

Figure 10: Hydrate morphology in a high methane leakage system. (a) No hydrate. (b) Hydrates first form on the surface of gas bubble and at grain contacts. (c) Hydrates form across the entire sample (mainly formed in the grain contact, a small amount is formed in the pore fluid). (d) The end of hydrate formation (with a methane leakage channel). S represents the sand grain. W represents water. H represents gas hydrate. G represents methane gas.

hydrate reservoirs, Cai et al. [38] proposed a very good fractal model based on fractal geometry theory. In this study, we performed calculations using the adjusted model and compared the measured results with the calculated results (Figure 9). In the methane flux system with the formation of hydrates, the distribution of gas and water in the deposition system should occur in different modes. Figure 9 shows the results for the homogeneous gas distribution (H) and the patchy gas distribution (P) when the new model is applied. When the hydrate saturation is 10-30%, the experimental data fall in the region between EMT-B (P) and EMT-B (H), and the test value of P-wave velocity is similar to mode EMT-B (H). At hydrate saturation of 30-60%, the test values are close to EMT-B (H), indicating that hydrate is formed along the grain contact surface and the gas in the system is uniformly distributed. At 60-70% saturation, the test values are close to the EMT-A model. After the hydrate saturation reaches more than 80%, the test values are close to mode EMT-B.

In the different micro-distribution modes, the hydrate will have different elastic effects on the hydrate-bearing sediments. It is also important to explore the distribution pattern of hydrate in sediments by using the link between the measured velocity and saturation, combined with the rock physics model. Based on the obtained experimental results and the comparative analysis with the theoretical model, the mechanism of hydrate formation in methane flux mode can be examined. From Figure 9, when the hydrate saturation is 10–60%, the hydrate mainly formed along grain contacts, which is an important stage of hydrate formation. Generally, when the free gas reaches suitable hydrate formation conditions, hydrate directly forms at the gas-water interface [39]. However, in this reaction system, it is difficult for hydrates to stably develop in pore spaces due to the presence of larger gases and fluid fluxes. Sediment particles, as a stable deposition medium, can provide a relatively stable environment for the formation of hydrates, thus exhibiting hydrate formation at this stage in the form of particle contact. When the hydrate saturation gradually increases, about 60–70%, the pore space is relatively small, and the hydrate gradually forms in the pore-filling mode. As hydrate continues to be generated, once the pore space has produced a large amount of hydrate, the hydrate generation pattern gradually develops toward the contact mode. In the case of a high methane flux leakage system, where the gas has a large influence on the elastic wave velocity of the hydrate-bearing sediments, the gas factor needs to be taken into account in the theoretical calculation. It is necessary to adjust the equivalent theoretical model to consider the influence of gas. The effective medium theory (EMT), which considers the gas factor, can not only estimate the hydrate saturation, but also help to predict the micro-distribution pattern of hydrate.

4.3. Hydrate Morphology in Methane Flux Mode. In the methane flux mode, the gas flow rate is set and the gas flows through the system at a set flow rate throughout the reactor. From the results of the previous investigation, it can be seen that the field methane flux is quite different from the methane flux used in experimental conditions. Laboratory conditions represent a high methane leakage system. Under such conditions, larger gas and fluid fluxes will make it more difficult for hydrates to be stably generated in pore fluids. The obtained experimental data and theoretical model calculation results show that hydrate is mainly formed along grain contacts at 10–60% saturation. And, the results are similar to mode EMT-A at 60–70% hydrate saturation. After 80% or more hydrate saturation, the calculated values are close to mode EMT-B.

Therefore, it is inferred that in the high methane flux leakage system, hydrates are first mainly formed by the grain contact mode (Figure 10), and then hydrates formed in the pore-filling mode. As the hydrate saturation increases, the hydrates in the fluid contact the sediment particles and the hydrates formed in the grain contact mode.

In the methane flux mode, high methane fluxes will form more hydrates around the gas bubbles. When the hydrate saturation is 10–60%, under the same hydrate saturation conditions, the higher the methane flux, the higher the shear modulus, and the greater the hydrate contribution to the sediment skeleton. (Figure 11). From the results calculated by the BGTL theoretical model, it can also be seen that the change of the parameter n can suitably reflect the changes in hydrate deposits. The parameter n is mainly related to the partial pressure and the consolidation degree of the sample. The smaller the value of n, the better the consolidation of the sample. It is clear that the larger the methane flux, the smaller the value of n, which indicates that the hydrate lends greater support to the sediment frame strength.

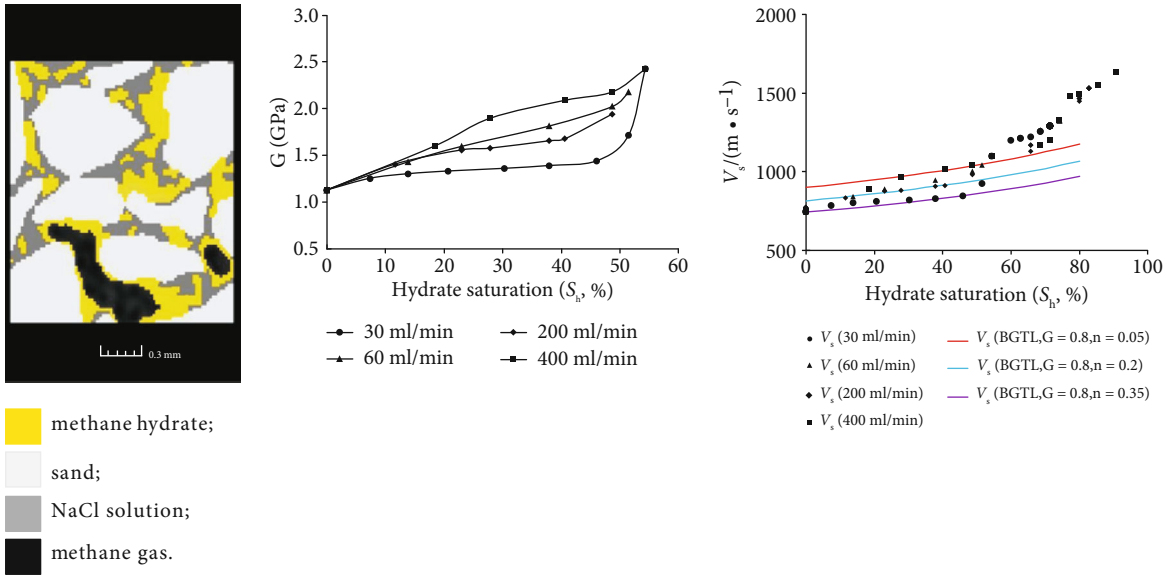

(a) (b) (c)

FIGURE 11: Hydrate distribution with changes in shear modulus and shear wave velocity. (a) Pore scale distribution of gas hydrates in sediments by X-CT (modified from [19]), (b) Variation in shear modulus with hydrate saturation in different methane flux, (c) Variation in S- wave velocities with hydrate saturation and analysis of the value of BGTL theory (Data for Figure 11 are in Table S10 in the Supplementary Materials).

5. Conclusions

The hydrate simulation experiments were conducted in different methane flux supply modes. The temperature, pressure, saturation, and wave velocities of the hydrate-bearing sediments were measured and the methane flux at the inlet side was controlled. The experimental data were analyzed and the model was verified. The main findings are:

(1) Smaller methane flux supplies result in less time required to generate the maximum hydrate, and the higher the methane flux, the more time is required to reach the maximum hydrate saturation. The hydrate formation rates are similar at different methane supply fluxes. The hydrate saturation reached 71.4% at a gas flow rate of 30 ml/min, and hydrate saturation reached 90.9% at an inlet flow rate of 400 ml/min. The larger the methane flux, the easier it is to form a high-saturation hydrate

(2) Model relationship between hydrate saturation and acoustic velocity in different methane flux models was established from the obtained experimental data. When hydrate first formed, the velocity increased slowly with hydrate saturation, while velocity increased quickly as the saturation reached 50–60%. The results are verified using different petrophysical equations, effective medium theory, and the BGTL theoretical model. The results show that the BGTL theory has good adaptability to the experimental results and can provide suggestions for the selection of model parameters. The effective medium theory is modified and adjusted, and the effective medium theory is used in gas- bearing conditions. The experimental values are more consistent with the theoretical results of EMT-B (homogenous gas distribution) at 10-60% hydrate saturation, and can provide some guidance regarding the morphology of the hydrate

(3) The hydrate morphology during this experiment was investigated. In the methane flux supply mode, the hydrate was mainly produced by particle contact mode in the gas flow supply mode, and hydrate mainly formed in grain contact mode when the hydrate saturation was 10–60%. As the hydrate saturation reached 60–70%, hydrate formed in the pore-filling mode, then the hydrate in the fluid gets contact with sediments, and finally the hydrate form at the grain contact. In the methane flux mode, the higher the methane flux, the higher the shear modulus, and the greater the hydrate contribution to the sediment skeleton

Data Availability

The data used in the article are in the supplementary materials. Data are available on request.

Conflicts of Interest

The authors declare that they have no conflicts of interest.

Acknowledgments

This research was supported financially by the National Natural Science Foundation of China (No. 41906067), the

Shandong Provincial Natural Science Foundation (No. ZR2019BD051), the Shandong Special Fund of Pilot National Laboratory for Marine Science and Technology (Qingdao) (No.2021QNLM020002), the China Postdoctoral Science Foundation (Grant No. 2018 M632634), the Shandong Province Postdoctoral Innovation Project (201902050), and also by the Marine Geological Survey Program (DD20221704).

Supplementary Materials

The Supplementary Materials contain text S1 and S2, Figure S1–S5, Table S1, S2 and S3. Text S1 and S2 introduce the measuring method of the acoustic data and hydrate saturation, separately. Figure S1-S3 exhibit the Calibration of the ultrasonic transducers. Figure S4 exhibits the Calibration of the TDR probes. Figure S5 exhibits the inner of the apparatus, especially for the microporous sintered plate. Table S1, S2 and S3 are the detail data of the calibration. And also the supporting information contains Table S4, S5, S6, S7, S8, S9 and S10. They are the detailed data of Figures 2, 3, 4–9, 11. *(Supplementary Materials)*

References

[1] Z. R. Chong, S. H. B. Yang, P. Babu, P. Linga, and X.-S. Li, "Review of natural gas hydrates as an energy resource: prospects and challenges," *Applied Energy*, vol. 162, pp. 1633–1652, 2016.

[2] Y. Li, C. He, N. Wu et al., "Laboratory Study on Hydrate Production Using a Slow, Multistage Depressurization Strategy," *Geofluids*, vol. 2021, Article ID 4352910, 13 pages, 2021.

[3] Y. Li, L. Liu, Y. Jin, and N. Wu, "Characterization and development of marine natural gas hydrate reservoirs in clayey-silt sediments: a review and discussion," *Advances in Geo-Energy Research*, vol. 5, no. 1, pp. 75–86, 2021.

[4] G. Hu, Y. Ye, J. Zhang, C. Liu, and Q. Li, "Acoustic response of gas hydrate formation in sediments from South China Sea," *Marine & Petroleum Geology*, vol. 52, no. 2, pp. 1–8, 2014.

[5] Q. Bu, G. Hu, C. Liu, T. Xing, C. Li, and Q. Meng, "Acoustic characteristics and micro-distribution prediction during hydrate dissociation in sediments from the South China Sea," *Journal of Natural Gas Science and Engineering*, vol. 65, pp. 135–144, 2019.

[6] J. Cai, W. Wei, X. Hu, and D. A. Wood, "Electrical conductivity models in saturated porous media: A review," *Earth-Science Reviews*, vol. 171, pp. 419–433, 2017.

[7] J. Cai, Z. Zhang, W. Wei, D. Guo, S. Li, and P. Zhao, "The critical factors for permeability-formation factor relation in reservoir rocks: Pore-throat ratio, tortuosity and connectivity," *Energy*, vol. 188, p. 116051, 2019.

[8] L. Liu, N. Wu, C. Liu et al., "Maximum Sizes of Fluid-Occupied Pores within Hydrate-Bearing Porous Media Composed of Different Host Particles," *Geofluids*, vol. 2020, Article ID 8880286, 14 pages, 2020.

[9] L. Liu, Z. Zhang, C. Li et al., "Hydrate growth in quartzitic sands and implication of pore fractal characteristics to hydraulic, mechanical, and electrical properties of hydrate-bearing sediments," *Journal of Natural Gas Science and Engineering*, vol. 75, p. 103109, 2020.

[10] N. Mahabadi, X. Zheng, T. S. Yun, L. Van Paassen, and J. Jang, "Gas bubble migration and trapping in porous media: Pore-scale simulation," *Journal of Geophysical Research: Solid Earth*, vol. 123, no. 2, pp. 1060–1071, 2018.

[11] K. E. Thatcher, G. K. Westbrook, S. Sarkar, and T. A. Minshull, "Methane release from warming-induced hydrate dissociation in the west svalbard continental margin: timing, rates, and geological controls," *Journal of Geophysical Research: Solid Earth*, vol. 118, no. 1, pp. 22–38, 2013.

[12] P. Wang, S. Wang, Y. Song, and M. Yang, "Methane Hydrate Formation and Decomposition Properties During Gas Migration in Porous Medium," *Energy Procedia*, vol. 105, pp. 4668–4673, 2017.

[13] J. A. Priest, A. I. Best, and C. R. I. Clayton, "A laboratory investigation into the seismic velocities of methane gas hydrate-bearing sand," *Journal of Geophysical Research: Solid Earth*, vol. 110, no. B4, 2005.

[14] J. A. Priest, E. V. L. Rees, and C. R. I. Clayton, "Influence of gas hydrate morphology on the seismic velocities of sands," *Journal of Geophysical Research: Solid Earth*, vol. 114, no. 11, 2009.

[15] W. J. Winters, W. F. Waite, D. H. Mason, L. Y. Gilbert, and I. A. Pecher, "Methane gas hydrate effect on sediment acoustic and strength properties," *Journal of Petroleum Science & Engineering*, vol. 56, no. 1-3, pp. 127–135, 2007.

[16] G. Hu, *Experimental Study on Acoustic Response of Gas Hydrates to Sediments from South China Sea [Ph. D. Thesis]*, Faculty of Earth Sciences, China University of Geosciences, Wuhan, China, 2010.

[17] G. Hu, Y. Ye, J. Zhang, C. Liu, S. Diao, and J. Wang, "Acoustic properties of gas hydrate–bearing consolidated sediments and experimental testing of elastic velocity models," *Journal of Geophysical Research: Solid Earth*, vol. 115, no. B2, 2010.

[18] G. Hu, Y. Ye, J. Zhang, S. Diao, and C. Liu, "Acoustic properties of hydrate-bearing unconsolidated sediments measured by the bender element technique," *Chinese Journal of Geophysics*, vol. 55, no. 6, pp. 635–647, 2012.

[19] G. Hu, C. Li, Y. Ye, C. Liu, J. Zhang, and S. Diao, "Observation of gas hydrate distribution in sediment pore space," *Chinese Journal of Geophysics*, vol. 57, no. 5, pp. 1675–1682, 2014.

[20] A. Andhumoudine, X. Nie, Q. Zhou et al., "Investigation of coal elastic properties based on digital core technology and finite element method," *Advances in Geo-Energy Research*, vol. 5, no. 1, pp. 53–63, 2021.

[21] Q. Gao, J. Zhao, Z. Yin, D. Yang, and C. Zhang, "Experimental study on methane hydrate formation in quartz sand under triaxial condition," *Journal of Natural Gas Science and Engineering*, vol. 85, p. 103707, 2020.

[22] Q. Gao, J. Zhao, Z. Yin, D. Yang, and C. Zhang, "Experimental study on fluid production from methane hydrate sediments under the marine triaxial condition," *Energy & Fuels*, vol. 35, no. 5, pp. 3915–3924, 2021.

[23] Q. Gao, Z. Yin, J. Zhao, D. Yang, and P. Linga, "Tuning the fluid production behaviour of hydrate-bearing sediments by multi-stage depressurization," *Chemical Engineering Journal*, vol. 406, p. 127174, 2020.

[24] M. Eaton, D. Mahajan, and R. Flood, "A novel high-pressure apparatus to study hydrate-sediment interactions," *Journal of Petroleum Science & Engineering*, vol. 56, no. 1-3, pp. 101–107, 2007.

[25] T. Kwon and G. Cho, "Evolution of compressional wave velocity during CO2Hydrate formation in sediments," *Energy & Fuels*, vol. 23, no. 11, pp. 5731–5736, 2009.

[26] B. Liu, H. Pan, X. Wang, F. Li, C. Sun, and G. Chen, "Evaluation of different CH_4-CO_2 replacement processes in hydrate-bearing sediments by measuring p-wave velocity," *Energies*, vol. 6, no. 12, pp. 6242–6254, 2013.

[27] J. Guan, D. Li, H. Zhou, D. Liang, and L. Wan, "A experimental system simulate formation and dissosiation of the leak gas hydrate," *Nature Gas Industry*, vol. 32, no. 5, pp. 1–4, 2012.

[28] Q. Bu, G. Hu, Y. Ye et al., "The elastic wave velocity response of methane gas hydrate formation in vertical gas migration systems," *Journal of Geophysics and Engineering*, vol. 14, no. 3, pp. 555–569, 2017.

[29] Q. Bu, G. Hu, C. Liu et al., "Effect of methane gas on acoustic characteristics of hydrate-bearing sediment-model analysis and experimental verification," *Journal of Ocean University of China*, vol. 20, no. 1, pp. 75–86, 2021.

[30] C. Liu, Y. Ye, S. Sun, Q. Chen, Q. Meng, and G. Hu, "Experimental studies on the P-T stability conditions and influencing factors of gas hydrate in different systems," *Science China Earth Sciences*, vol. 56, no. 4, pp. 594–600, 2013.

[31] J. Wright, F. Nixon, S. Dallimore, and O. Matsubayashi, *A method for direct measurement of gas hydrate amounts based on the bulk dielectric properties of laboratory test media paper presented at 4th International Conference on Gas Hydrates*, Tokyo Institute of Technology, Yokohama, Japan, 2002.

[32] C. Li, G. Hu, W. Zhang et al., "Influence of foraminifera on formation and occurrence characteristics of natural gas hydrates in fine-grained sediments from Shenhu area, South China Sea," *Science China Earth Sciences*, vol. 59, no. 11, pp. 2223–2230, 2016.

[33] C. Li, C. Liu, G. Hu et al., "Investigation on the multiparameter of hydrate-bearing sands using nano-focus X-ray computed tomography," *Journal of Geophysical Research: Solid Earth*, vol. 124, no. 3, pp. 2286–2296, 2019.

[34] J. Dvorkin, M. Prasad, A. Sakai, and D. Lavoie, "Elasticity of marine sediments: rock physics modeling," *Geophysical Research Letters*, vol. 26, no. 12, pp. 1781–1784, 1999.

[35] M. B. Helgerud, J. Dvorkin, A. Nur, A. Sakai, and T. Collett, "Elastic-wave velocity in marine sediments with gas hydrates: effective medium modeling," *Geophysical Research Letters*, vol. 26, no. 13, pp. 2021–2024, 1999.

[36] T. Ahrens, *Mineral Physics & Crystallography: a handbook of physical constants*, Published by American Geophysical union, 1995.

[37] J. Cai, Y. Xia, S. Xu, and H. Tian, "Advances in multiphase seepage characteristics of natural gas hydrate sediments," *Chinese Journal of Theoretical and Applied Mechanics*, vol. 52, no. 1, pp. 208–223, 2019.

[38] J. Cai, Y. Xia, C. Lu, H. Bian, and S. Zou, "Creeping microstructure and fractal permeability model of natural gas hydrate reservoir," *Marine and Petroleum Geology*, vol. 115, p. 104282, 2020.

[39] E. Spangenberg, M. Priegnitz, K. Heeschen, and J. M. Schicks, "Are laboratory-formed hydrate-bearing systems analogous to those in nature?," *Journal of Chemical & Engineering Data*, vol. 60, no. 2, pp. 258–268, 2015.